



Three-Dimensional Cellular Structures Enhanced by Shape Memory Alloys

*Michael V. Nathal and David L. Krause
Glenn Research Center, Cleveland, Ohio*

*Nathan G. Wilmoth
Vantage Partners, LLC, Brook Park, Ohio*

*Brett A. Bednarczyk
Glenn Research Center, Cleveland, Ohio*

*Eric H. Baker
Connecticut Reserve Technologies, Inc., Cleveland, Ohio*

NASA STI Program . . . in Profile

Since its founding, NASA has been dedicated to the advancement of aeronautics and space science. The NASA Scientific and Technical Information (STI) program plays a key part in helping NASA maintain this important role.

The NASA STI Program operates under the auspices of the Agency Chief Information Officer. It collects, organizes, provides for archiving, and disseminates NASA's STI. The NASA STI program provides access to the NASA Aeronautics and Space Database and its public interface, the NASA Technical Reports Server, thus providing one of the largest collections of aeronautical and space science STI in the world. Results are published in both non-NASA channels and by NASA in the NASA STI Report Series, which includes the following report types:

- **TECHNICAL PUBLICATION.** Reports of completed research or a major significant phase of research that present the results of NASA programs and include extensive data or theoretical analysis. Includes compilations of significant scientific and technical data and information deemed to be of continuing reference value. NASA counterpart of peer-reviewed formal professional papers but has less stringent limitations on manuscript length and extent of graphic presentations.
- **TECHNICAL MEMORANDUM.** Scientific and technical findings that are preliminary or of specialized interest, e.g., quick release reports, working papers, and bibliographies that contain minimal annotation. Does not contain extensive analysis.
- **CONTRACTOR REPORT.** Scientific and technical findings by NASA-sponsored contractors and grantees.

- **CONFERENCE PUBLICATION.** Collected papers from scientific and technical conferences, symposia, seminars, or other meetings sponsored or cosponsored by NASA.
- **SPECIAL PUBLICATION.** Scientific, technical, or historical information from NASA programs, projects, and missions, often concerned with subjects having substantial public interest.
- **TECHNICAL TRANSLATION.** English-language translations of foreign scientific and technical material pertinent to NASA's mission.

Specialized services also include creating custom thesauri, building customized databases, organizing and publishing research results.

For more information about the NASA STI program, see the following:

- Access the NASA STI program home page at <http://www.sti.nasa.gov>
- E-mail your question to help@sti.nasa.gov
- Fax your question to the NASA STI Information Desk at 443-757-5803
- Phone the NASA STI Information Desk at 443-757-5802
- Write to:
STI Information Desk
NASA Center for AeroSpace Information
7115 Standard Drive
Hanover, MD 21076-1320



Three-Dimensional Cellular Structures Enhanced by Shape Memory Alloys

*Michael V. Nathal and David L. Krause
Glenn Research Center, Cleveland, Ohio*

*Nathan G. Wilmoth
Vantage Partners, LLC, Brook Park, Ohio*

*Brett A. Bednarczyk
Glenn Research Center, Cleveland, Ohio*

*Eric H. Baker
Connecticut Reserve Technologies, Inc., Cleveland, Ohio*

National Aeronautics and
Space Administration

Glenn Research Center
Cleveland, Ohio 44135

Trade names and trademarks are used in this report for identification only. Their usage does not constitute an official endorsement, either expressed or implied, by the National Aeronautics and Space Administration.

Level of Review: This material has been technically reviewed by technical management.

Available from

NASA Center for Aerospace Information
7115 Standard Drive
Hanover, MD 21076-1320

National Technical Information Service
5301 Shawnee Road
Alexandria, VA 22312

Available electronically at <http://www.sti.nasa.gov>

Three-Dimensional Cellular Structures Enhanced by Shape Memory Alloys

Michael V. Nathal and David L. Krause
National Aeronautics and Space Administration
Glenn Research Center
Cleveland, Ohio 44135

Nathan G. Wilmoth
Vantage Partners, LLC
Brook Park, Ohio 44142

Brett A. Bednarczyk
National Aeronautics and Space Administration
Glenn Research Center
Cleveland, Ohio 44135

Eric H. Baker
Connecticut Reserve Technologies, Inc.
Cleveland, Ohio 44040

Abstract

This research effort explored lightweight structural concepts married with advanced “smart” materials to achieve a wide variety of benefits in airframe and engine components. Lattice block structures were cast from an aerospace structural titanium alloy Ti-6Al-4V and a NiTi shape memory alloy (SMA), and preliminary properties have been measured. A finite element-based modeling approach that can rapidly and accurately capture the deformation response of lattice architectures was developed. The Ti-6-4 and SMA material behavior was calibrated via experimental tests of ligaments machined from the lattice. Benchmark testing of complete lattice structures verified the main aspects of the model as well as demonstrated the advantages of the lattice structure. Shape memory behavior of a sample machined from a lattice block was also demonstrated.

1.0 Introduction

The technical literature abounds with lightweight structural concepts using periodic cellular structures such as honeycombs and lattice block materials. Honeycombs have been primarily used in lightweight sandwich structures and are some of the most efficient (high strength/density) structures in many important loading situations such as bending (Ref. 1). Lattice block, consisting of truss architectures (Fig. 1) at a micro- or meso-scale, are preferred over honeycombs (Fig. 2) when the loading situations are more three-dimensional, or when honeycomb fabrication is not compatible with the desired material selection (Ref. 2). Lattice block structures are also damage and defect tolerant (Ref. 3) and can be efficient in heat transfer; for example, cooling fluid can be passed through the lattice. In the past five years, an exciting outgrowth of these concepts is the development of “auxetic” structures (Fig. 2(b)), which are characterized by negative structural Poisson’s ratios (indicating that a structure gets thicker when it is stretched, the opposite of normal behavior). Scarpa and co-workers (Refs. 4 to 6) applied an auxetic structure to airfoil shapes (Fig. 3) and showed that a wing box with an auxetic core offers high deformability while maintaining structural integrity, which is particularly attractive for morphing behavior. High amounts of camber change were both predicted and measured. Ju and Summers (Refs. 7 to 10) also showed that auxetic structures have unusually high combinations of strength and compliance. Auxetics are also projected to have improved impact resistance and therefore have relevance to fan containment systems.

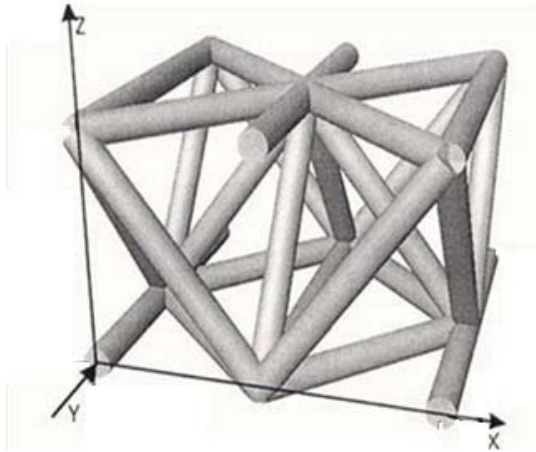


Figure 1.—Example lattice block unit cell.

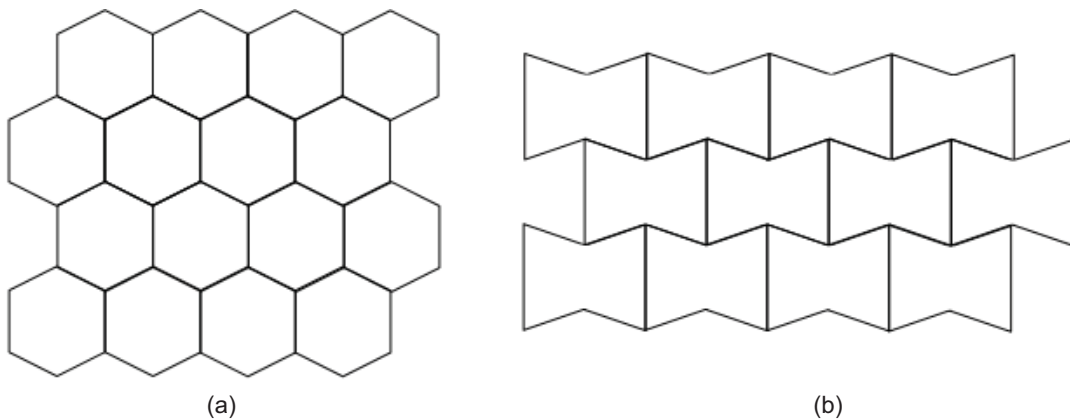


Figure 2.—Example honeycomb structure configurations: (a) conventional, and (b) auxetic.

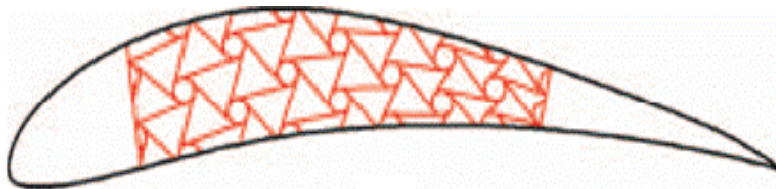


Figure 3.—Auxetic morphing airfoil from Spadoni and Ruzzene (Ref. 5).

Constructing the cellular structures from shape memory alloys (SMAs) provides even greater potential. SMAs can be used in two ways, depending on alloy selection and temperature (Ref. 11). First, SMAs can be designed to take advantage of the shape memory effect. Here, the structure can change shape as a response to heating and cooling cycles to achieve morphing behavior, or alternately a self-healing concept where damage from an impact event can be recovered via a thermal treatment. Secondly, SMAs can be designed to be superelastic. Extremely high deformations and loads can be achieved while still behaving in a reversible manner similar to an elastic response (and thereby allowing long lives and durability in fatigue, gust and impact loading situations).

Prior work on lattice block materials has included work on investment castings to produce net shape lattice castings. This allows for parts with complex curvatures to be easily fabricated. Aluminum alloys (Ref. 12), nickel-based superalloys (Ref. 3), and titanium alloys (Ref. 13) have been examined. In general, the ability of the casting process to produce quality castings was demonstrated, although the tendency for porosity resulting from solidification shrinkage was difficult to eliminate. Despite significant casting defects, good strength and damage tolerance of the lattice structures have been measured.

The purpose of the present work was to explore the structural performance of lattice structures fabricated by investment casting. Evaluation of both conventional and auxetic lattices, using both an SMA and an aerospace structural Ti alloy (Ti-6wt% Al-4%V) was planned. The castings were produced by Transition45 Technologies Inc., Orange, California, which developed the casting process under a Small Business Innovative Research contract with NASA (Ref. 14). The details of their casting development are considered proprietary and are restricted to the contract reports. This report will cover the mechanical property evaluation of the castings produced by T45. Note that auxetic lattice structures were not produced in time for inclusion in this report, and therefore no further discussion is provided.

2.0 Material Processing

The SMA castings received to date had a higher population of casting defects than T45 would normally deliver, but NASA elected to receive these in order to get at least a preliminary indication of SMA lattice behavior. Cracks were the most significant defect, and occurred particularly at lattice nodes. The particular composition for this work, Ni-50at% Ti, was chosen because of its very high shape memory actuation capacity. However, this alloy is not optimally processed by casting, and substantial amounts of the deleterious Ti_2Ni phase were found during microscopic characterization of the castings. Attempts to minimize this embrittling phase by modifying the casting parameters are in progress. If these trials are unsuccessful, a new Ni-rich alloy (Ni-49.8at % Ti) may be the best choice for future castings. Defects were present in the Ti-6-4 castings also, but at a much lower occurrence than in the SMA castings. In general, our experience with the lattice structure test articles revealed that the large surface area and configuration of the cellular casting make non-destructive inspection for determining the presence of all cracks and defects rather difficult.

3.0 Ligament Testing

Both 90° and 45° ligaments were machined from the Ti-6-4 and SMA lattice blocks in preparation for testing, as shown in Figure 4. Note that these test samples included lattice nodes (see circled regions, Fig. 4(b)), which are a common site for casting defects. These unconventional geometries required a new clamping grip system to be designed to match the ligament shapes in order to test in tension. Duplicate tension and compression tests of Ti-6-4 ligaments at 23, 165, and 200 °C were completed. Representative stress-strain curves are shown in Figures 5 and 6, respectively. The stress and strain scales are fixed for all tests to highlight the change in properties with an increase in test temperature.

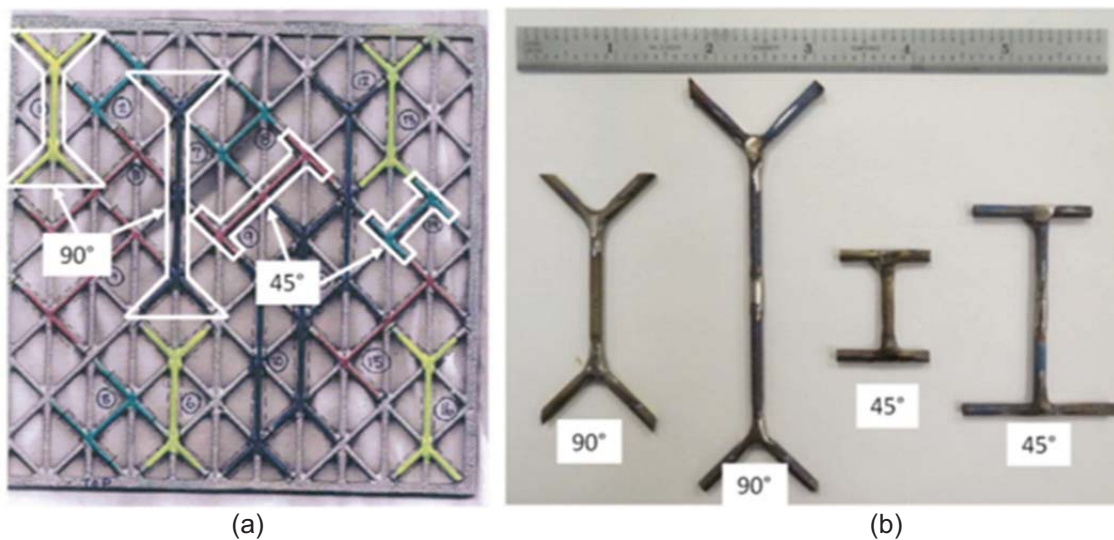
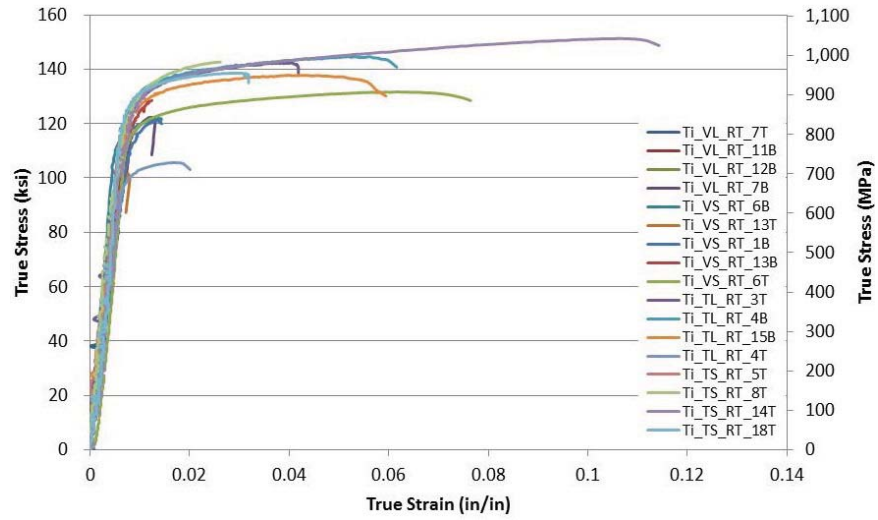
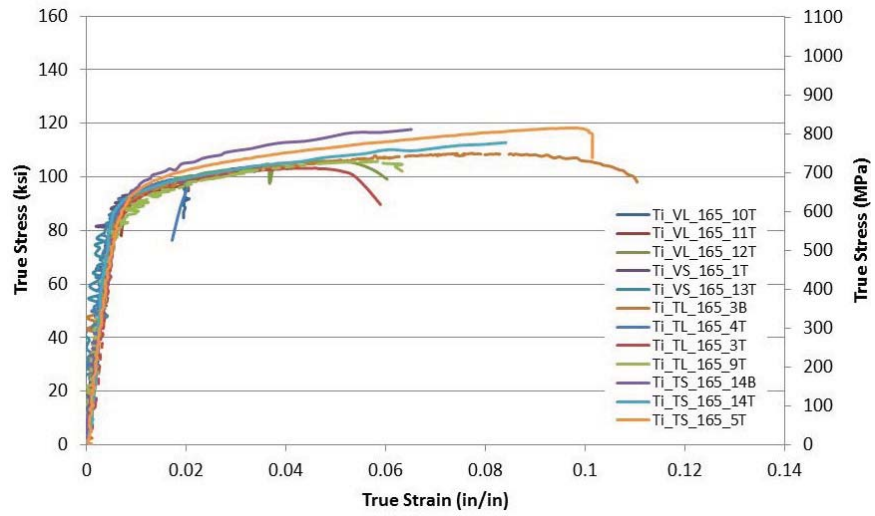


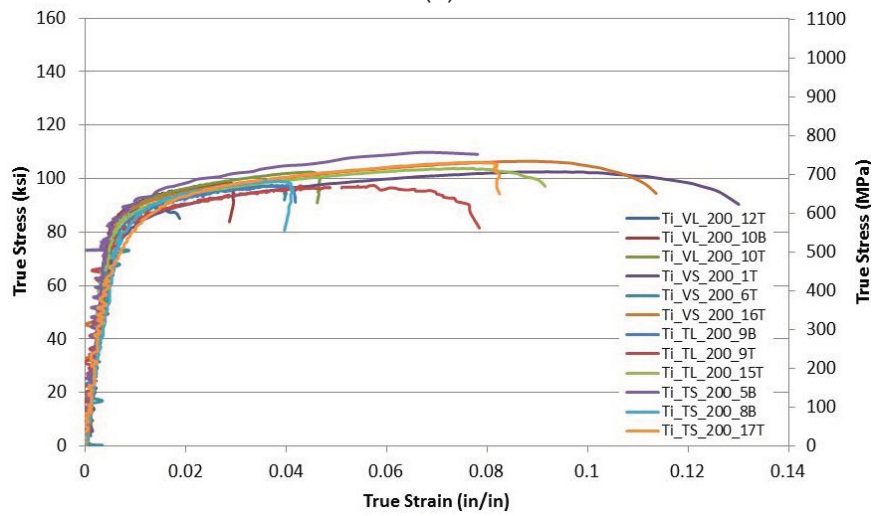
Figure 4.—(a) Lattice block bulk casting, and (b) machined ligament specimens for tensile testing.



(a)



(b)



(c)

Figure 5.—Ti-6-4 tension testing stress-strain curves at (a) 23 °C, (b) 165 °C, and (c) 200 °C.

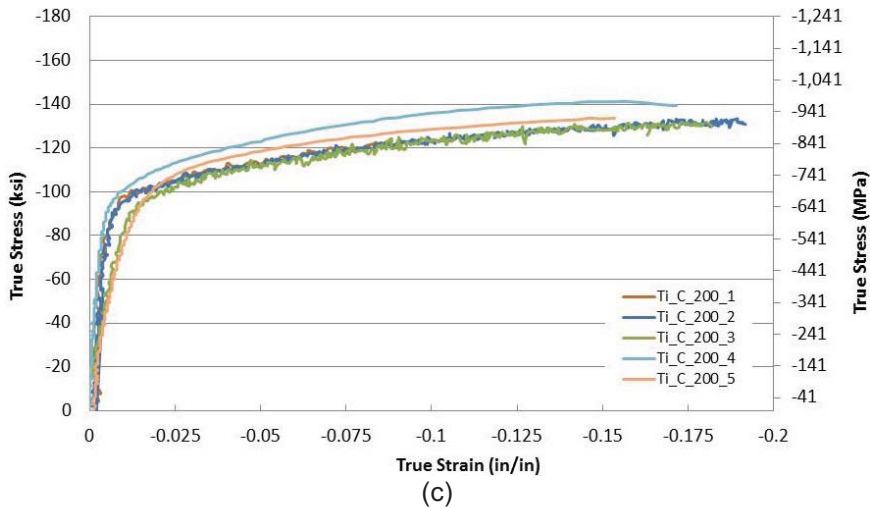
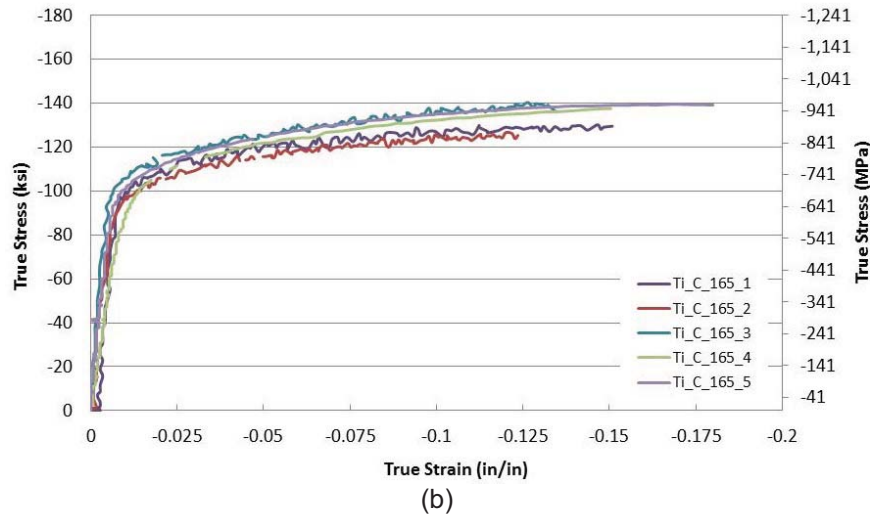
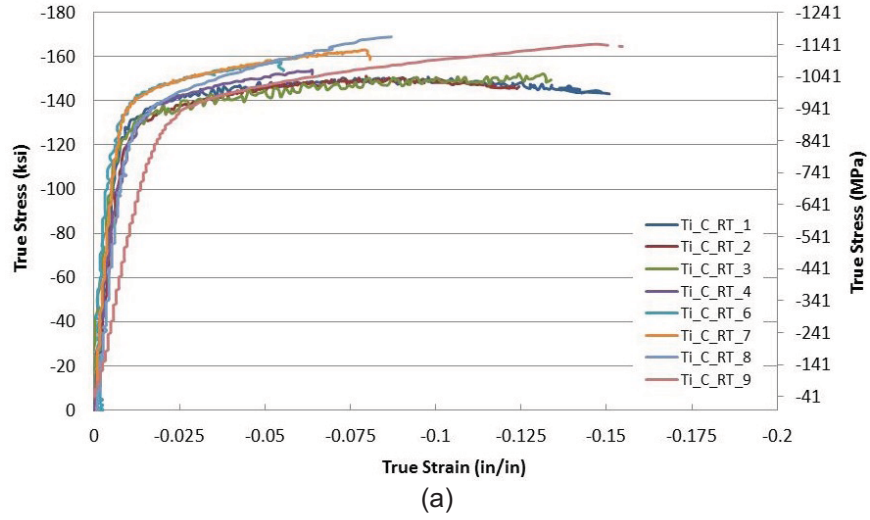


Figure 6.—Ti-6-4 compression stress-strain curves at (a) 23 °C, (b) 165 °C, and (c) 200 °C.

TABLE 1.—SUMMARY OF LIGAMENT TENSILE AND COMPRESSION DATA

Test temp. (°C)	Material	Test type	Elastic modulus (GPa) ^a	Yield stress (MPa) ^b	Ultimate strength (MPa)	Poisson's ratio	Literature source or experimental data
23	Ti-6-4	tension	114	897	1000	0.26 to 0.36	Refs. 15 & 16
165	Ti-6-4	tension	107	700	828	0.26 to 0.36	Refs. 15 & 16
200	Ti-6-4	tension	105	679	786	0.26 to 0.36	Refs. 15 & 16
23	Ti-6-4	tension	117	830	929	0.3	as measured
165	Ti-6-4	tension	105	612	743	0.31	as measured
200	Ti-6-4	tension	101	562	695	0.31	as measured
23	Ti-6-4	compression	113	870	x	0.33	as measured
165	Ti-6-4	compression	109	673	x	0.34	as measured
200	Ti-6-4	compression	87	642	x	0.34	as measured
23	Ni-50%Ti	compression	36.1	-240	-425		Ref. 17
23	Ni-50%Ti	compression	28	-249	-475		as measured
165	Ni-50%Ti	compression	51	-474			as measured
200	Ni-50%Ti	compression	49	-564			as measured

^aFor compression tests of the Ni-50%Ti material, this is the stress at initial apparent yielding

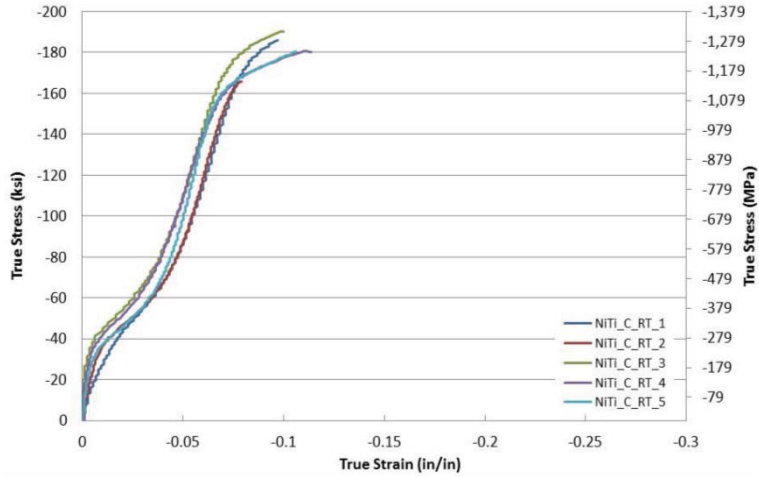
^bFor compression tests of the Ni-50%Ti material, this is the stress at the finish of reorientation

A summary of the material properties for Ti-6-4 tests obtained from literature and the averages of this testing effort are shown in Table 1. In general, the measured strengths were found to differ only slightly from published data (Refs. 15 and 16) for conventionally processed materials. This indicates that the casting process produced acceptable microstructures. Some tensile ligaments exhibited early failure, which was most likely due to casting defects. Note that the elastic moduli of the 200 °C compression tests were lower than expected, because a large percentage of those specimens exhibited buckling failures.

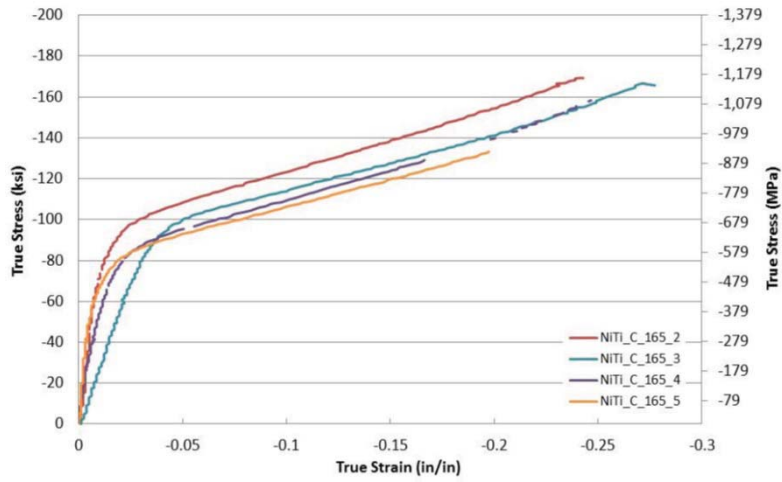
Duplicate tension and compression testing at 23, 165, and 200 °C were also envisioned for ligaments extracted from SMA lattice block panels. Because of the casting problems mentioned previously, only compression samples could be extracted from the SMA panels. The representative stress-strain curves for these tests are shown in Figure 7. There is scatter in the data. The expected curve shapes are observed, however. At room temperature, the stress strain curves exhibit an initial yielding which is considered the onset of martensite reorientation and detwinning (Refs. 17 and 18). Martensite reorientation continues at a slight hardening rate for approximately 0.5 percent strain, followed by a region with steeply increased hardening, which is associated with plastic deformation of the martensite (Refs. 17 and 18). At the higher test temperatures, the alloy is austenitic and the yielding behavior corresponds to stress-induced martensite and concurrent operation of slip and deformation twinning (Ref. 19).

For the NiTi base SMAs, a large amount of tensile data is available in the literature but very little data is available for compression testing. Room temperature compression testing completed by other NASA groups on extruded NiTi (Ref. 17) was located and used for comparison to current as-cast test results in Table 1. The moduli from the as-cast specimens from this test effort are lower compared to the extruded material by 22.3 percent. Note that the initial yielding and reorientation finish stresses are slightly higher than as reported for the extruded material.

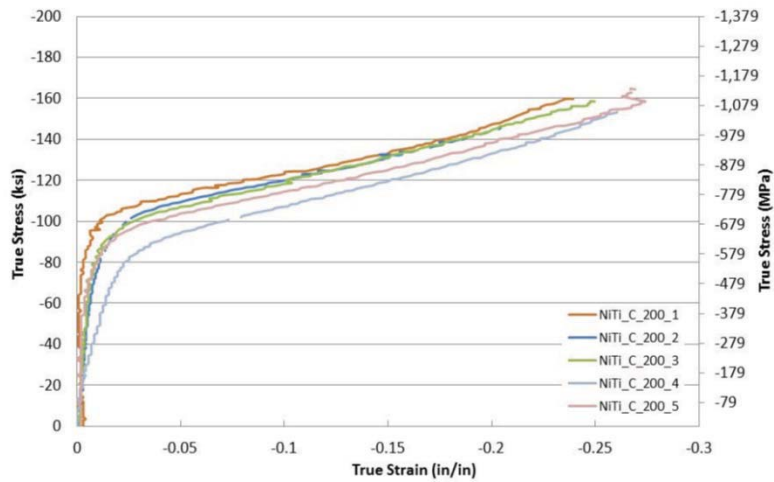
Ligament testing results were used as calibration data for the finite element modeling, as described in Figure 8. In addition, the SMA specimen compressed at room temperature was subsequently heated to evaluate shape memory behavior. Approximately 3 percent strain was recovered upon heating, which is consistent with the expected behavior of the alloy.



(a)

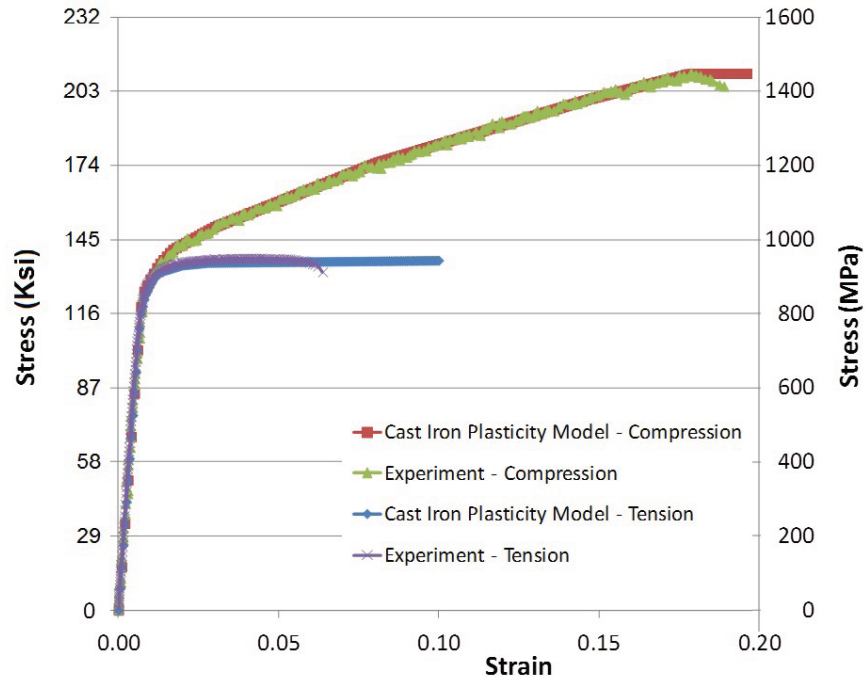


(b)

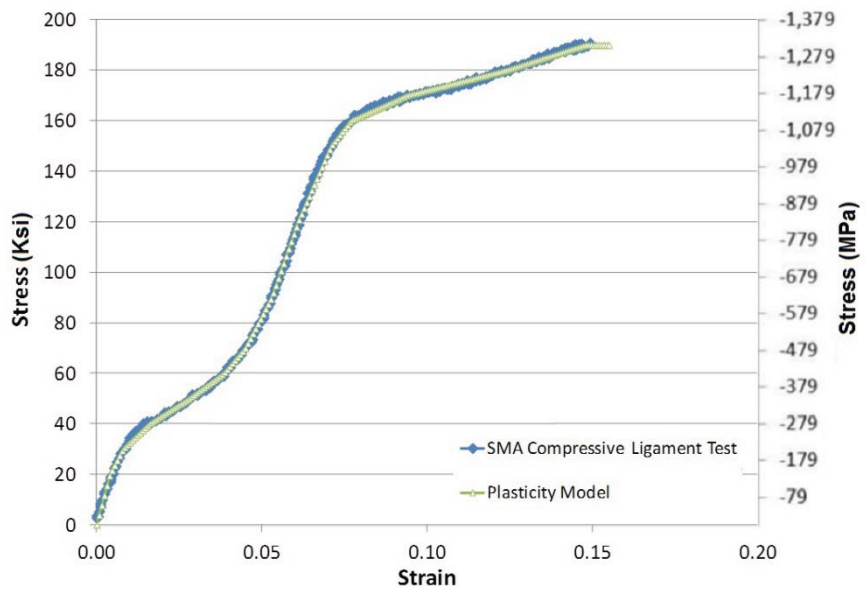


(c)

Figure 7.—NiTi compression stress-strain curves at (a) 23 °C, (b) 165 °C, and (c) 200 °C.



(a)



(b)

Figure 8.—Ligament test results with material calibration curve fits to existing Abaqus constitutive models: (a) Ti-6-4 in tension and compression, and (b) SMA in compression.

4.0 Model Development

The purpose of the modeling effort was to ensure that a proper understanding of the physics of lattice deformation had been achieved. This then would allow for high confidence in future extrapolations to new structures as well as in optimization of the lattice structure geometry for particular applications. Low cost evaluation of multiple structural concepts before investing in experimental demonstration efforts would be a key benefit.

A Python script was written to automatically generate Abaqus (Dassault Systèmes) finite element models of arbitrary lattice geometries. The script was parametric, so it was quick and efficient to generate models for different configurations, run finite element models, and post-process results. The ligaments were treated as beams with arbitrary nonlinear material behavior that can also experience nonlinear geometric effects. Example lattice geometries generated using the Python script are shown in Figure 9.

The script was then specialized to generate models of the 4-point bend and flat-wise compression tests that were conducted. The acreage ligament cross-section was treated as circular, while the edge ligament cross-section was treated as rectangular to match the as-fabricated conditions. Pre-test predictions, along with parametric sensitivity studies, were conducted for the 4-point bend configuration of the Ti-6-4 lattice. The 4-point bend test article and model geometry are shown in Figure 10.

After performing a mesh sensitivity study to arrive at a globally converged mesh, a parametric sensitivity study was performed by varying the material representation, the height of the panel, and the ligament diameter. At the time of the pre-test predictions, only tensile ligament test results were available, showing some variability. The nonlinear material response was modeled using von Mises plasticity. To capture the variability in the tensile test results, two sets of material data were used in the sensitivity studies, as shown in Figure 11.

Variation of the panel height was intended to examine the effect of non-centered ligament nodes in the as-built lattice panels. This is shown in Figure 12. To assess the impact of this offset, panel heights (distances between face ligament centroids) of 18.0 and 21.5 mm were examined.

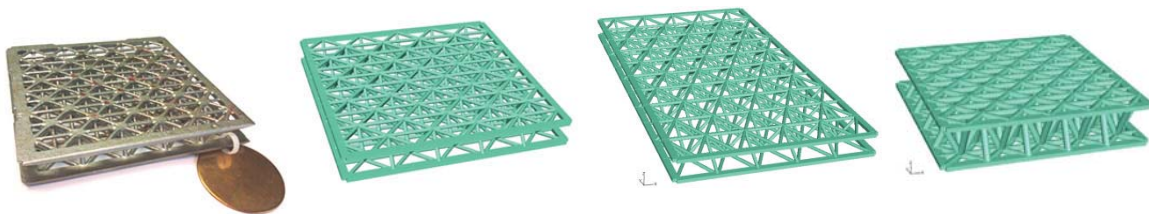
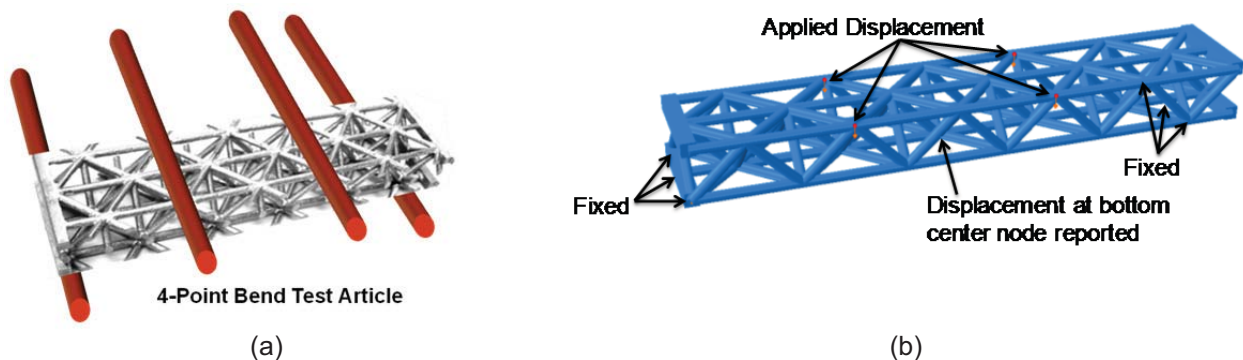


Figure 9.—Actual lattice casting and three sample geometries generated with the Python Script.



(a) (b)
Figure 10.—(a) 4-point bend test article, and (b) finite element model.

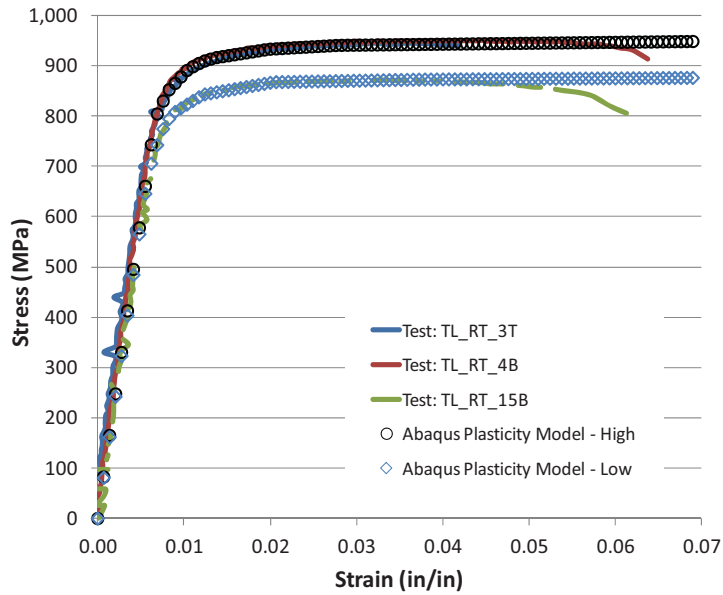


Figure 11.—Abaqus plasticity model fit to room-temperature Ti-6-4 ligament test data that was used to capture the variability of the material response.

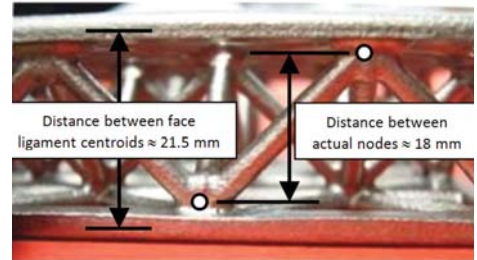


Figure 12.—Offset between face ligament centroids and actual node location.

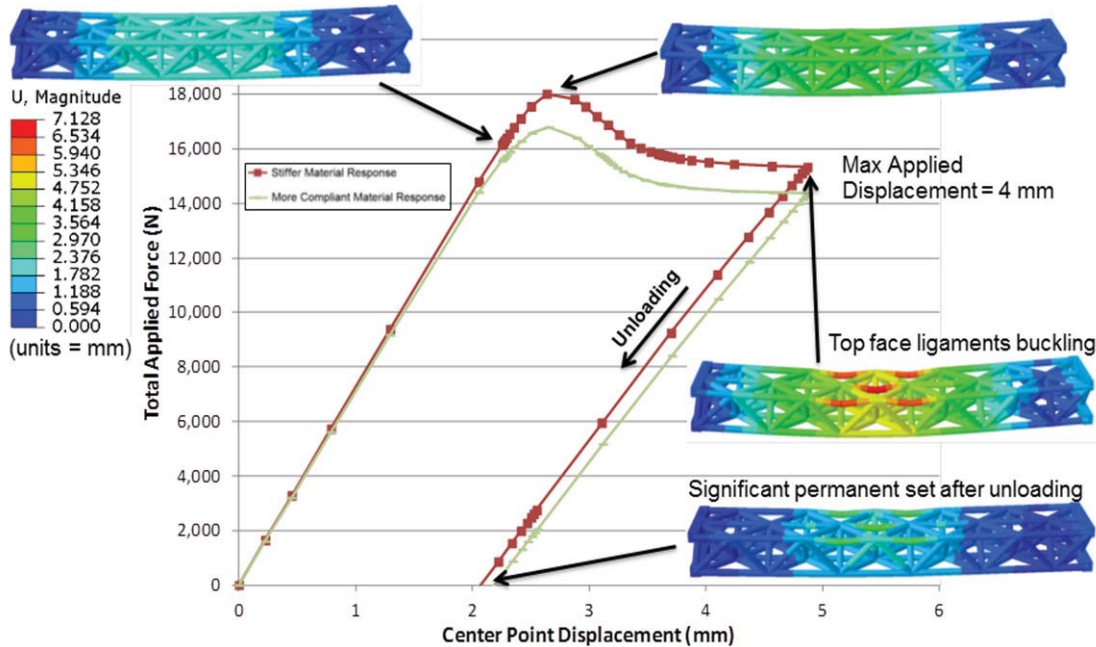


Figure 13.—Pre-test prediction of Ti-6-4 lattice block 4-point bend response.

Finally, ligament diameters of 3.25, 3.50, and 3.75 mm were examined to assess the impact of cross-sectional area variability, which has been observed in the lattice ligaments. The predicted applied load versus bottom center point deflection is plotted in Figure 13, along with deformation contours at various points. These two curves represent what was then believed to be the best pre-test predictions while still factoring in the variable Ti-6-4 material response shown in Figure 11. The predicted response involved a peak, followed by softening as significant buckling of the top face struts was predicted. The model was loaded in displacement control of top face points (Fig. 10) to a maximum of 4 mm, then unloaded. A significant amount of permanent set, due to plasticity, was predicted.

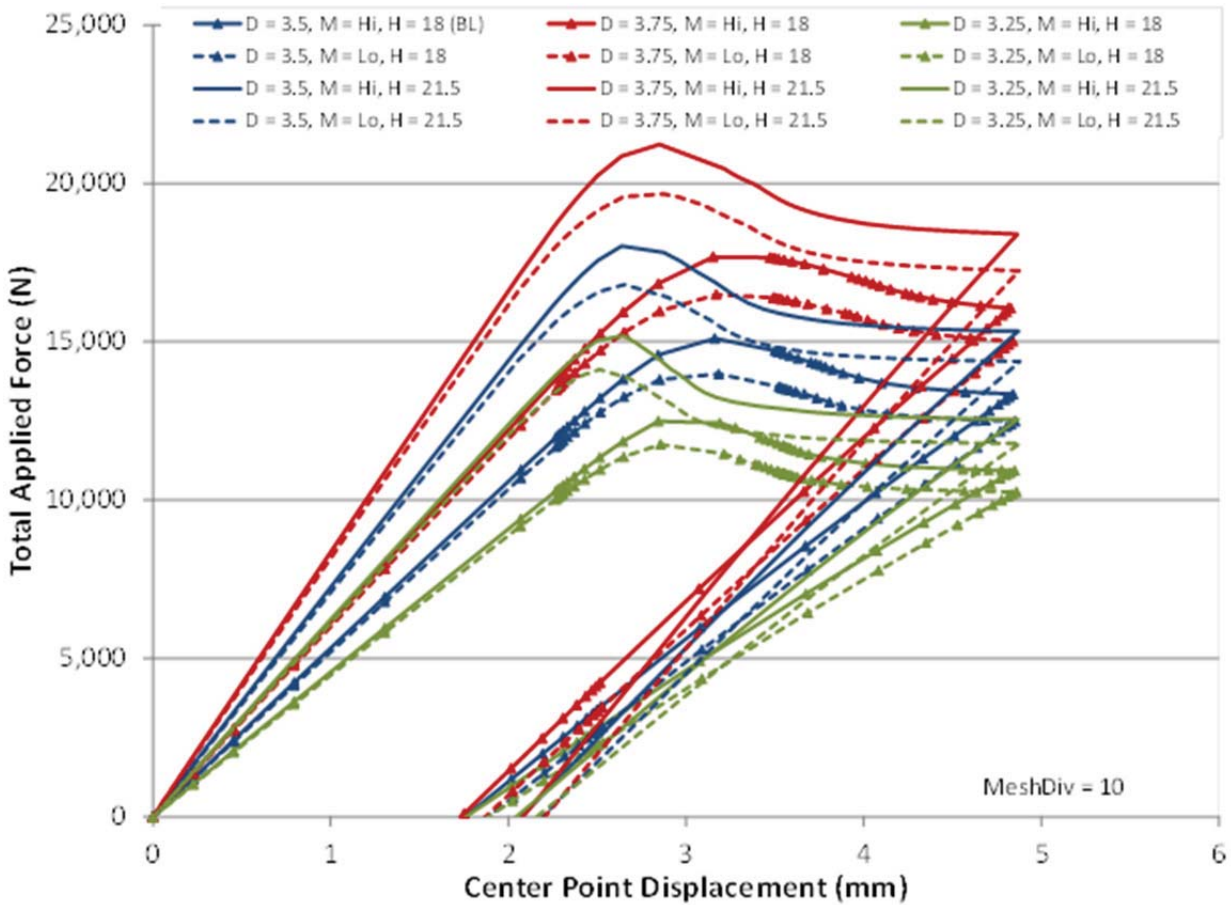


Figure 14.—Full set of parametric simulations on the 4-point bend response of the Ti-6-4 Lattice.

The full set of results from the parametric study, where panel height, Ti-6-4 material representation, and ligament diameter were varied, is shown in Figure 14. These results indicated that panel height and strut diameter had a significant effect on the lattice 4-point bend response (changes on the order of 35 percent), while the Ti-6-4 material variation examined was minor (changes on the order of 5 percent). This is not surprising, as deflection and load carrying capacity in this test configuration are structural in nature—that is, governed by rigidity (elastic modulus E times bending moment of inertia I) rather than material stiffness (proportional to E) alone and the cross sectional area of each strut. Note that I is highly nonlinear with height h : for example, $I = bh^3/12$ for a plate or laminate, where b is the representative width.

5.0 Structural Benchmark Testing

The structural benchmark testing effort included mechanical tests of complete lattice structure test articles. By evaluating the mechanical response to prototypical structural loadings, this work provided physical evidence of advantages in the lattice cellular structure configuration. Some of these advantages were light weight, high efficiency, and inherent structural redundancy. In addition, the testing demonstrated shape memory response in a complex lattice structure, which augmented understanding the effect observed in the tests from the simpler geometry of solid uniaxial test coupons. As described in the next section, the tests also provided data for verification of the soundness of the model development effort.

Testing was based on availability of lattice castings. Lattice structures cast in Ti-6-4 were received in two configurations: 100 by 100 by 25 mm panels, and a 50 by 200 by 25 mm panel. The former were retained for future flat-wise compression testing, while the latter was cut into three long-beam bending test articles. Lattice structures cast in the SMA NiTi were also received, in the 100 by 100 by 25 mm panel configuration. These were suitable for flat-wise compression tests. All test series were conducted isothermally at room temperature (23 °C).

The first test series was performed on Ti-6-4 Test Article S/N 22C. This test article had overall dimensions of 200 by 50 by 25 mm and was 12 by 3 unit cells, composing three longitudinal “trusses.” The average strut diameter was 3.505 mm. The long-beam bend test configuration (Fig. 15) on the 50 kN MTS (MTS Systems Corporation) load frame was symmetrical. The lower reaction supports were placed at two-node locations spaced 180 mm apart, and the upper load rollers were placed at two-node locations spaced 72 mm apart. Four-point loading positioned the entire middle span between load rollers under the same nominal maximum moment value. In bending, the test article’s structural limits were explored through a series of increasing load ramp cycles in displacement control (Fig. 16). Elastic loadings to 2.224, 4.448, and 13.34 kN total load were completed with almost no measurable nonlinearity or hysteresis upon return to zero load. The elastic series was followed by loading to the first observed strut failure occurring at 20.01 kN (Fig. 17).

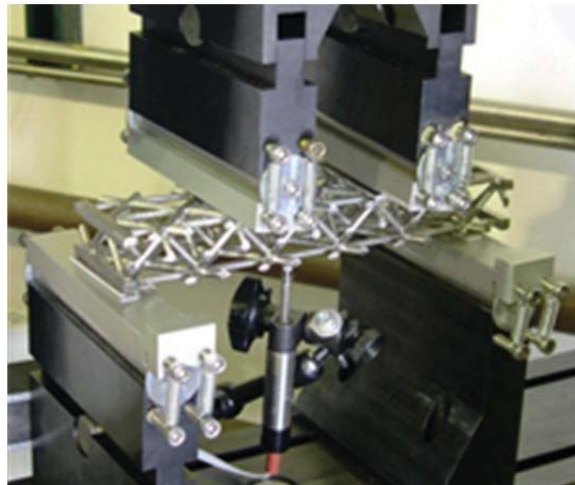


Figure 15.—Long-beam bend test set-up: lattice structure test article is shown mounted in hinged four-point load fixtures.

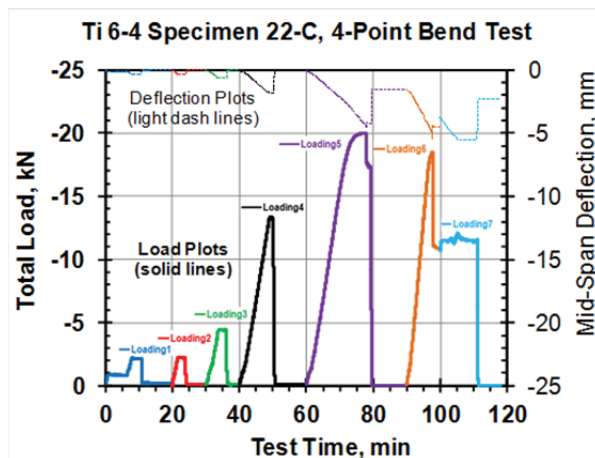


Figure 16.—Bend test load ramps: a series of bend test load ramps were applied to the lattice structure beam.

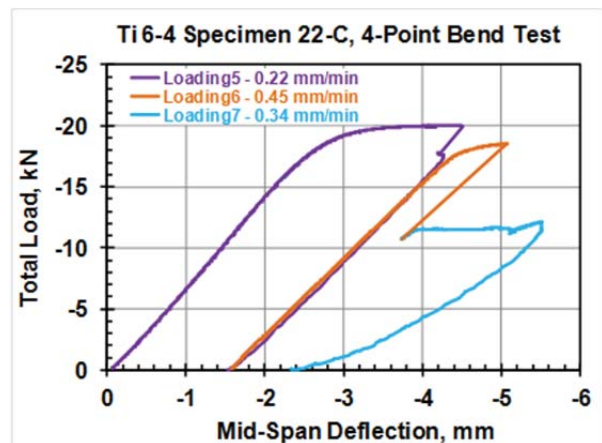


Figure 17.—Failure and residual strength tests: after first failure, most lattice structure strength remained.

With the displacement load ramp continuing to run for a short period, the specimen resisted approximately 17.5 kN. Upon unloading, specimen inspection using optical microscopy could not locate a suspected fracture. Additional residual strength testing was continued under test machine displacement control, until 18.49 kN strength was measured at the second strut failure. With the displacement loading continuing to run, residual strength of 12 kN was observed until the machine stroke limit of 5.5 mm specimen deflection was reached. Close post-test visual inspection revealed two fractures, one at a node and one through a strut.

The second test series was performed on SMA NiTi Test Article Heat 1131 S/N 2-1. This test panel had overall dimensions of 98 by 99 by 26 mm and was five unit cells square. The average strut diameter was 3.858 mm. The flat-wise compression strength test was performed first on a 50 kN MTS load frame and included a spherical joint fixture with rigid platens to assure uniform loading of all 18 upper and 18 lower “face sheet” nodes (Fig. 18(a)). Figure 18(b) provides a schematic showing the construction features of a spherical joint platen, which allows relative rotation between the upper and lower load surfaces.

In compression, the test frame’s load limit was approached prior to significant deformation or failure of the test article. A peak loading of 41.9 kN was recorded at 0.41 mm panel deflection. To further explore the load-carrying ability of the SMA test article, a 450 kN-capacity Instron load frame was reconfigured with the spherical joint platen fixtures. Upon loading, first failure was identified at 155 kN total panel load. An in situ inspection revealed a crack in the specimen’s integrally cast lower perimeter tension frame, likely at a pre-existing flaw. Continued higher loading under stroke control demonstrated load redistribution capability within the lattice structure, providing additional strength to achieve the peak load of 170 kN at 1.6 mm deflection. This deflection correlates to approximately 6 percent structural through-thickness deformation (Fig. 19). Note that the use of one linear variable differential transformer (LVDT) as positioned to measure displacement between the upper and lower platens may cause error in reported deflection if rotation of the spherical joint platen occurs due to unsymmetrical specimen stiffness. This may have contributed to the apparent increasing stiffness observed during Test1 Load as well as the apparent high stiffness observed upon the initial loading of Test2 Load seen in Figure 19. The potential discrepancy may be avoided by use of three LVDT’s to measure planar position changes, or by the use of one central LVDT to obtain the average deflection values. Post-test visual inspection revealed

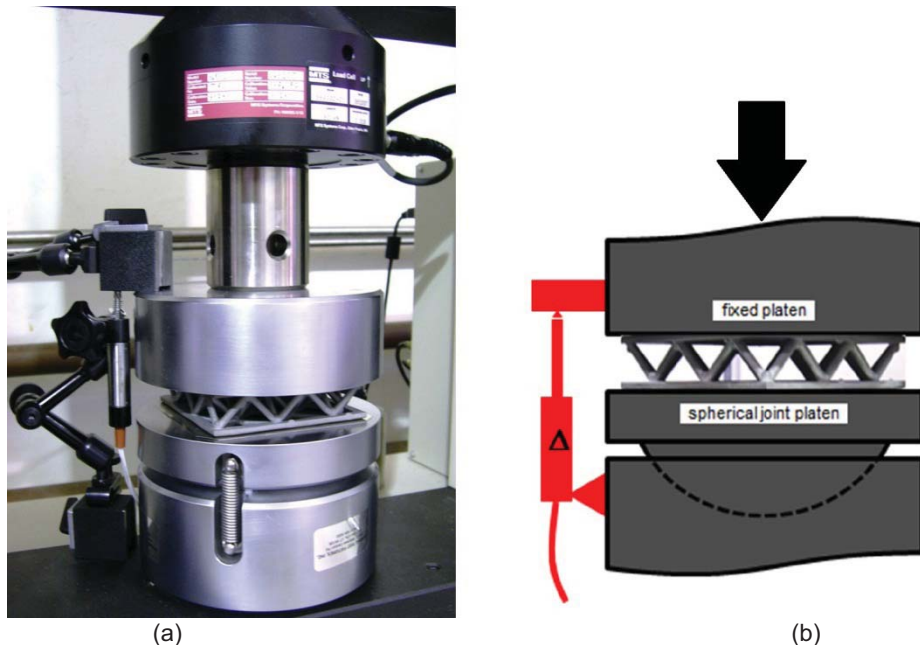


Figure 18.—Flat-wise compression test: (a) lattice test article is mounted between platens, with spherical joint fixture beneath specimen, and (b) schematic of spherical joint platens construction.

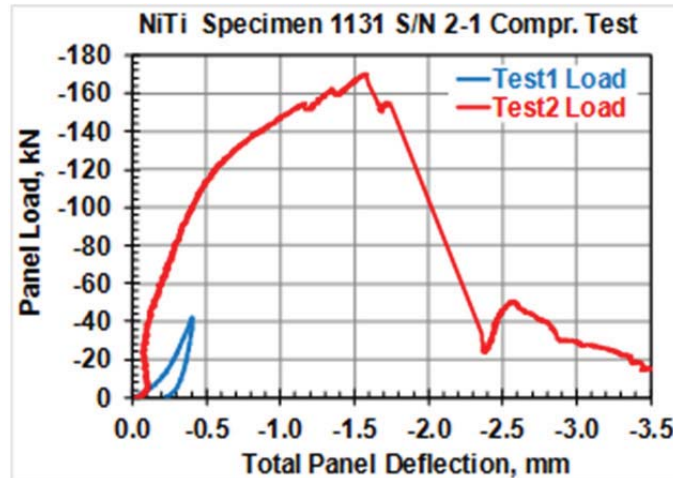


Figure 19.—Compression strength test of NiTi lattice: strength and deformation were available after the initial break at 155 kN.

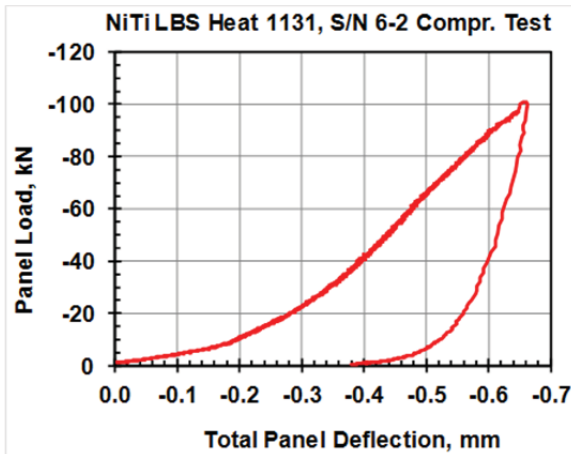


Figure 20.—Compression yield test: the second SMA lattice structure test article was loaded in compression to produce approximately 2 percent residual deformation.

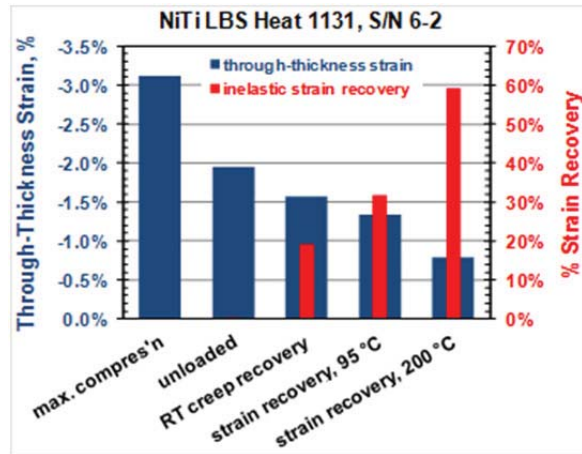


Figure 21.—Recovery of strain via the shape memory effect: thermal treatment restored 60 percent of the initial inelastic strain resulting from compression of the test article.

additional cracks in the upper and lower perimeter tension frames. This altered the structure’s stress distribution, placing struts in bending and progressively failing most nodes and cracking many struts at mid-length locations. Because of the extensive non-reversible damage, post-test thermal treatment for strain recovery (self-healing) was not warranted for this test article.

The third test series was performed on SMA NiTi Test Article Heat 1131 S/N 6-2. This test panel was cast to very similar overall dimensions and geometry as Test Article S/N 2-1. It had overall dimensions of 98 by 99 by 26 mm and was five unit cells square. The average strut diameter was 3.858 mm. The flat-wise compression yield test with strain recovery was performed on the 450 kN-capacity Instron load frame configured with the spherical joint and platen fixtures (similar to Fig. 18). In compression at a rate of 0.305 mm per minute, a peak load of 101 kN was attained at a deflection of 0.65 mm. This deflection corresponds to a 3.1 percent compressive structural strain (Fig. 20).

No evidence of cracking or failure of the structure was observed. Following release of the load, the residual compressive through-thickness strain was 1.95 percent. This value relaxed to 1.58 percent after a period of 15 min at room temperature. Post-test heat treatment at 95 °C resulted in strain recovery to 1.33 percent, while an additional heat treatment at 200 °C for 120 min produced strain recovery to 0.79 percent. This value of recovery is the equivalent of 60 percent of the initial inelastic deformation after release of the load (Fig. 21). This confirms shape memory behavior in the structural lattice.

6.0 Analytical Verification

The agreement between the most representative pre-test prediction (for average strut diameter of 3.5 mm) and the bend test performed on the Ti-6-4 lattice is shown in Figure 22. As shown, the model predicted the initial slope and onset of nonlinearity well, but the softening associated with top ligament buckling was absent in the test data. In the test, failure occurred in one of the two ligaments in the bottom face as shown. Note that no attempt to model this type of ligament fracture had yet been made. The lack of softening in the test results indicated that buckling of the top face struts was limited in the test and overpredicted in the model.

In an attempt to explain the discrepancy, compressive ligament test data, which became available after the 4-point bend test, was modeled using an existing material model in the Abaqus library (“cast iron plasticity model”). This model allows for distinct tensile and compressive material plastic behavior. The fit of the model to experimental room-temperature Ti-6-4 ligament data is shown in Figure 8, where now the compressive response hardened significantly more than the tensile response (Fig. 8(a)). Switching to this material model decreased but did not eliminate the amount of softening in the model (Fig. 23). To further suppress the buckling in the top face ligaments, a non-circular ligament cross-section was considered in the top face of the lattice only. This simulated the tear-drop shaped cross-section of the casting (Fig. 23) and enabled the ligaments to have greater resistance to out-of-plane bending and thus greater buckling resistance. For simplicity, a rectangular cross-section was considered as shown in Figure 23.

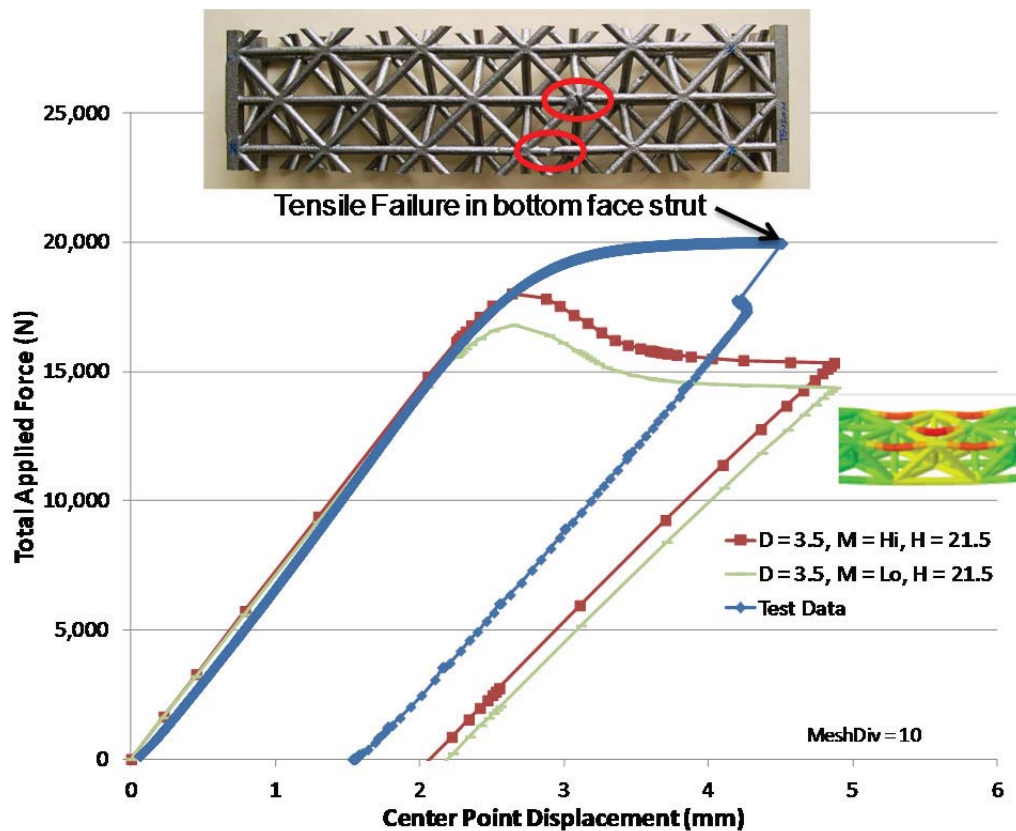


Figure 22.—Correlation between pre-test prediction and Ti-6-4 lattice block 4-point bend test data.

Figure 23 compares the altered model with the experimental data. While the rectangular shape of the top face ligaments was not completely representative, this simulation showed that by suppressing buckling of the top face ligaments, the test data could be captured. An additional feature that would also suppress top face ligament buckling was the thicker ligament sections near the nodes, which was not included in the model geometry. This would reduce the free span of the ligaments, which would reduce their tendency to buckle. This effect will be examined in the future.

Finally, a pre-test prediction was made for the flat-wise compression behavior of the SMA lattice. The actual casting and the Abaqus model are shown in Figure 24. To simulate the flat-wise compression test, the bottom nodes in the model were fixed and the top nodes were displaced downward at a constant rate. As a first step, the SMA material was modeled using the Abaqus von Mises plasticity constitutive model. The fit of this model to SMA ligament tensile test data is shown in Figure 8. The agreement between the pre-test flat-wise compression prediction and experiment is shown in Figure 25. The model matched the experiment well for the initial slope and onset of nonlinearity. The model was then slightly more compliant than the test data. The model response began to stiffen in association with the SMA material stiffening response shown in Figure 8. The model was then not able to converge due to the extensive buckling of the lattice internal ligaments. Although this cannot necessarily be considered a predicted failure, it did occur at an applied displacement of 1.18 mm, which corresponds closely to the applied displacement at first failure in the test (1.16 mm).

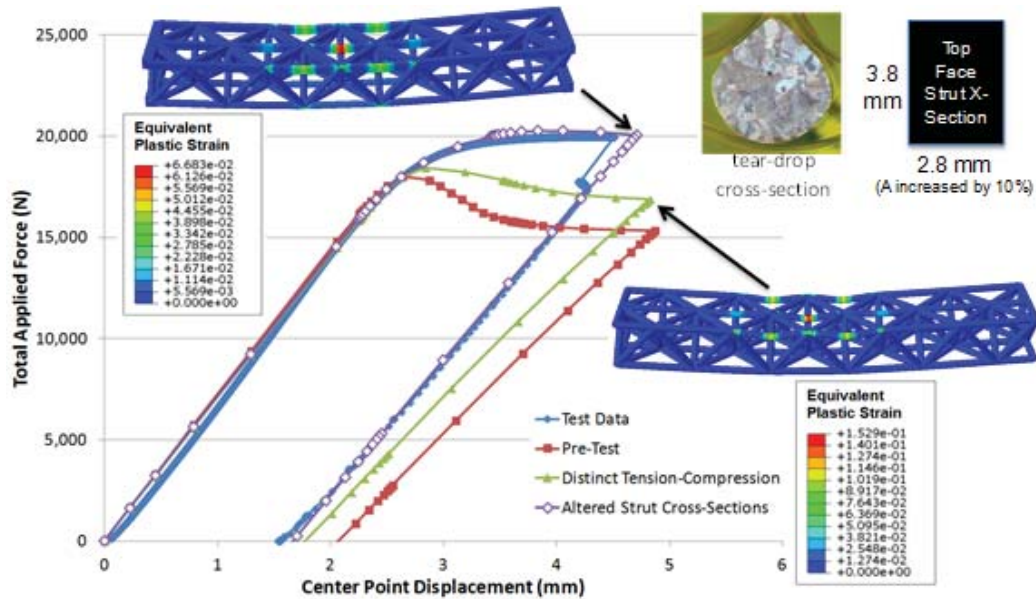


Figure 23.—Correlation of model, altered to suppress top face ligament buckling, with experiment for the Ti-6-4 lattice 4-point bend test.



Figure 24.—(a) SMA lattice casting, and (b) Abaqus finite element model.

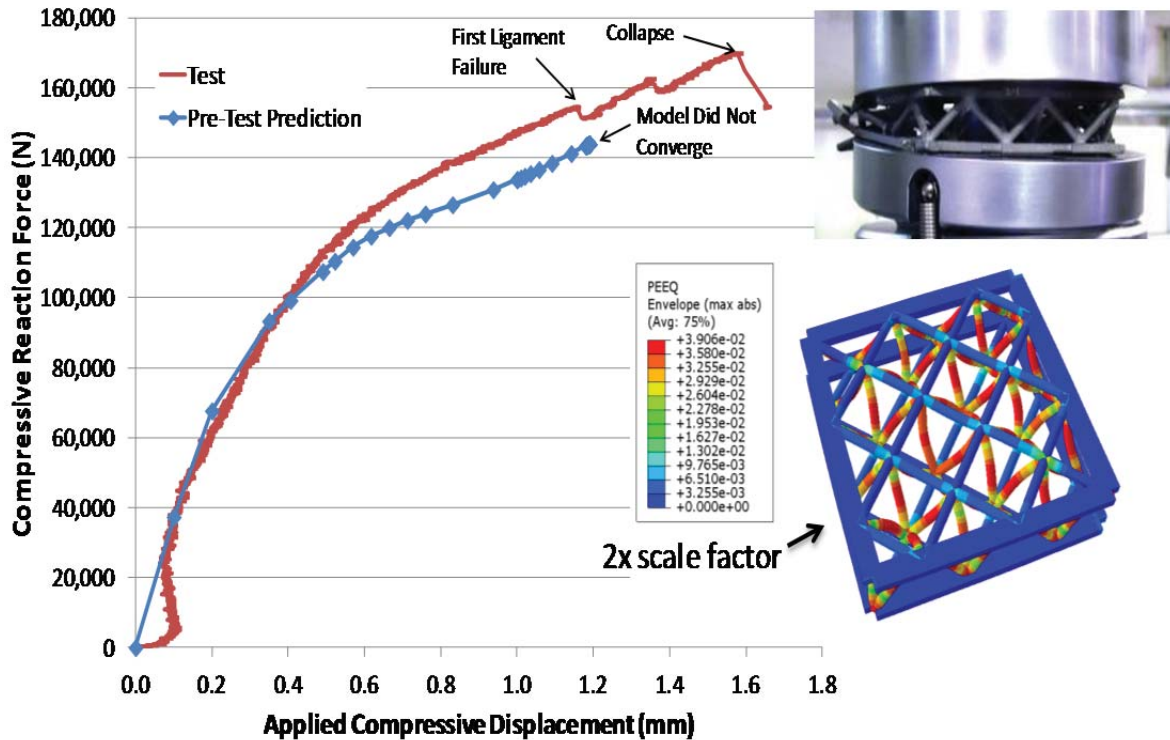


Figure 25.—Model prediction and experimental results for SMA lattice in compression.

7.0 Summary and Conclusions

This paper explores the performance of lattice block structures and their suitability for aerospace applications. Lattice blocks were cast from aerospace structural titanium alloy Ti-6Al-4V and NiTi shape memory alloy. Preliminary properties have been measured as a part of this test effort. A finite element-based modeling approach that can rapidly and accurately capture the deformation response of lattice architectures was developed. The Ti-6-4 and SMA material behavior was calibrated via experimental tests of ligaments machined from the lattice. Benchmark testing of complete lattice structures verified the main aspects of the model as well as demonstrated the advantages of the lattice structure. Shape memory behavior of a sample machined from a lattice block was also demonstrated.

The long-beam bend testing of a Ti-6-4 lattice structure exhibited almost no inelastic behavior for loadings to 13.34 kN. This indicates that micro-yielding at local stress risers, if it existed, did not affect the overall structural response. After the first and second tensile failures of a strut (or node), much strength and deformation capability existed. The strength retention demonstrates the advantages of the highly redundant lattice structure the availability of alternative load paths after a failure. In bending, the top compression struts plastically deformed and buckled before the first bottom strut tensile rupture was discovered. For aerospace service this is a valuable benefit, because it provides an observable sign of distress before structural failure. Necking deformation at strut tensile breaks indicated fully developed plasticity above the Ti-6-4 material's yield point. As a testing consideration, the observed large specimen deformations required careful selection of the appropriate load and support fixtures to permit free rotations and lateral movements.

Flat-wise compression testing of SMA NiTi lattice structures indicated insensitivity to defects for this load case. The test articles had several known casting defects present but until failure of the integral tensile frame in one case, the defects did not affect test results to a measurable degree. In the first compression test article, 0.2 mm of deformation were unrecovered upon unloading from 41.9 kN during the first load cycle. Local yielding resulting from non-planar outer contact surfaces of the panel are the

most likely cause for the unrecovered deformations. Similarly, this may be responsible for the condition of initial increasing stiffness with load during the compression tests. For the first compression test article, the compliance curve of the second load cycle to 41.9 kN was greatly different than for the first cycle. This is a unique behavior characteristic of the SMA material. For the second compression test article, the recovery of 60 percent of the initial inelastic strain through heat treatment was representative of the shape memory effect. The high value of structural deformation at peak strength load capacity of the SMA test article further indicated an opportunity for high strain recovery (self-healing) upon thermal treatment.

Using material parameters calibrated by ligament testing, the finite element modeling captured all of the main features of the lattice block deformation behavior, including deviations from non-linearity, strut buckling, lattice geometric effects, and even indications of strut fracture. The model can be used to design new lattice blocks that are optimized for weight and structural performance.

References

1. Evans, A.G.: *Lightweight Structures and Materials*. October 2001, s.l.: MRS Bulletin, 2001, Vol. 36, p. 795.
2. Evans, A.G.; et al.: *The Topological Design of Multifunctional Cellular Metals*. [.pdf] s.l.: Progress in Materials Science, 2001. Vol. 46. pp. 310-326.
3. Nathal, M.V.; Whittenberger, J.D.; Hebsur, M.G.; Kantzos, P.T.; and Krause, D.L.: *Superalloy Lattice Block Structures*. Proc. 10th Intl. Symp on Superalloys, ed. by K.A. Green et al., The Minerals, Metals & Materials Society, 2004. pp. 431-440.
4. Martin, J.; Heyder-Bruckner, J.J.; Remillat, C.; Scarpa, F.; Potter, K.; and M. Ruzzene: *The Hexachiral Prismatic Wingbox Concept*. Phys. Stat. Sol. (b) 245, No. 3, 570–577 (2008).
5. Spadoni, A; and Ruzzene, M.: *Static Aeroelastic Response of Chiral-core Airfoils*. J. of Intelligent Material Systems and Structures, Vol. 18 (2007) p. 1067-1075.
6. Bettini, P.; Airoidi, A.; Sala, G.; Di Landro, L.; Ruzzene, M.; and Spadoni, A.: *Composite Chiral Structures for Morphing Airfoils: Numerical Analyses and Development of a Manufacturing Process*. Composites Part B, Vol. 41(2010), p. 133-147.
7. Ju, J.; Thompson, L.; Seera, N.; and Summers, J.: *Vibration and Damping of Hexagonal Honeycomb Sandwich Plates*. Proc. ASME Int. Mechanical Engineering Congress and Exposition, ASME (2010).
8. Schultz, J; Summers, J.; Ju, J.; and Thompson, L.: *A Simulational Study of the Dynamic Crushing of Conventional and Auxetic Honeycombs*. Proc. ASME Int. Mechanical Engineering Congress and Exposition, ASME (2010).
9. Ju, J.; and Summers, J.: *Hyperelastic Constitutive Modeling of Hexagonal Honeycombs Subjected to In-Plane Shear Loading*. J. Engineering Materials and Technology, Vol. 133 (2011) p. 011005-1 - 011005-8.
10. Ju, J.; and Summers, J.: *Compliant Hexagonal Periodic Lattice Structures Having Both High Shear Strength and High Shear Strain*. Materials and Design, Vol. 32 (2011) p. 512-524.
11. Nathal, M.V.; and Stefko, G.L.: *Smart Materials and Active Structures*. J. Aerosp. Eng. 2013.26:491-499.
12. Sypeck, D.J.; and Wadley, H.N.G.: *Cellular Metal Truss Core Sandwich Structures*. Advanced Engineering Materials, 2002, Vol. 4, pp. 759-764.
13. Li, Q.; Chen, E.Y.; Bice, D.R.; and Dunand, D.C.: *Mechanical Properties of Cast Ti-6Al-4V Lattice Block Structures*. Metallurgical and Materials Transactions, February 2008. Vol. 39A. pp. 441-449.
14. Chen, E.L.: *Shape Memory Alloy Based Periodic Cellular Structures*. NASA Contract NNX11CA42C, Transition45 Inc., 1739 N.Case Street, Orange, CA 92865.
15. Allegheny Technologies, Incorporated: *ATI Titanium 6Al-4V Alloy Technical Data Sheet*. 2010.
16. *ASM Materials Properties Handbook: Titanium Alloys*. Materials Park, ASM International, 1994, pp. 492-634.

17. Benafan, O.; Padula II, S.A.; Noebe, R.D.; Sisneros, T.A.; and Vaidyanathan, R.: Role of B19' Martensite Deformation in Stabilizing Two-Way Shape Memory Behavior in NiTi. *J. Appl. Phys.*, 2012. 112, 093510.
18. Stebner, A.P.; Brown, D.W.; and Brinson, L.C.: Young's Modulus Evolution and Texture-Based Elastic-Inelastic Strain Partitioning During Large Uniaxial Deformations of Monoclinic Nickel-Titanium. *Acta Mater.* 61, 2013. 1944-1956.
19. Benafan, O.; Noebe, R.D.; Padula II, S.A.; Garg, A.; Clausen, B.; Vogel, S.C.; and Vaidyanathan, R.: Temperature Dependent Deformation of B2 Austenite in a NiTi Shape Memory Alloy. *Int. J. Plast.*, 2013. <http://dx.doi.org/10.1016/j.ijplas.2013.06.003>.

